



LAWRENCE  
LIVERMORE  
NATIONAL  
LABORATORY

LLNL-TR-666552

# Projection Microstereolithography for Architected Materials

M. Shusteff

January 28, 2015

## Disclaimer

---

This document was prepared as an account of work sponsored by an agency of the United States government. Neither the United States government nor Lawrence Livermore National Security, LLC, nor any of their employees makes any warranty, expressed or implied, or assumes any legal liability or responsibility for the accuracy, completeness, or usefulness of any information, apparatus, product, or process disclosed, or represents that its use would not infringe privately owned rights. Reference herein to any specific commercial product, process, or service by trade name, trademark, manufacturer, or otherwise does not necessarily constitute or imply its endorsement, recommendation, or favoring by the United States government or Lawrence Livermore National Security, LLC. The views and opinions of authors expressed herein do not necessarily state or reflect those of the United States government or Lawrence Livermore National Security, LLC, and shall not be used for advertising or product endorsement purposes.

This work performed under the auspices of the U.S. Department of Energy by Lawrence Livermore National Laboratory under Contract DE-AC52-07NA27344.

# Projection Microstereolithography for Architected Materials (MIT EECS - RQE Written Report)

by

Maxim Shusteff

## RQE Committee:

Prof. Karl K. Berggren, chair

Prof. Dimitri Antoniadis

## Thesis Supervisor:

Prof. Nicholas X. Fang (Mechanical Engineering)

---

## TABLE OF CONTENTS

<b>1</b>	<b>Introduction: Overview of Stereolithography.....</b>	<b>2</b>
<b>2</b>	<b>Projection Microstereolithography .....</b>	<b>2</b>
2.1	<i>Unique Features of P<math>\mu</math>SL at LLNL.....</i>	<b>3</b>
2.1.1	LED Illumination .....	3
2.1.2	LCoS Spatial Light Modulator.....	3
2.1.3	P $\mu$ SL Build Process.....	4
2.2	<i>P<math>\mu</math>SL System Enhancements.....</i>	<b>4</b>
2.2.1	Real-time focusing feedback.....	4
2.2.2	Build-time illumination .....	5
2.2.3	Ambient Oxygen Control and Substrate Stability .....	6
2.3	<i>Polymerization Depth Study.....</i>	<b>7</b>
<b>3</b>	<b>Application of P<math>\mu</math>SL to Microarchitected Materials .....</b>	<b>9</b>
3.1	<i>Mechanical Properties of Low-density Materials .....</i>	<b>9</b>
3.1.1	Density-Dependent Scaling of Elastic Modulus and Strength.....	9
3.1.2	Stretch-Dominated Architectures and the Octet Truss .....	10
3.1.3	Significance of P $\mu$ SL-Fabricated Metamaterial Properties .....	10
3.2	<i>Breakthrough-Enabling Capability of P<math>\mu</math>SL.....</i>	<b>11</b>
<b>4</b>	<b>Conclusions and Outlook.....</b>	<b>12</b>
<b>5</b>	<b>References .....</b>	<b>13</b>

# 1 Introduction: Overview of Stereolithography

Stereolithography (SL) is a prominent paradigm in the realm of additive manufacturing (AM) technologies, which refers to fabrication approaches that build “bottom up” by adding material. Pioneered in 1984 by Chuck Hull [1], SL relies on light-activated solidification of a liquid photosensitive resin in a layer-by-layer fashion, with the geometry of each layer defined by sectioning a three-dimensional (3D) computer model by closely-spaced parallel planes. The maturation of the technology over nearly three subsequent decades has resulted in the wide availability of commercial SL products, such as the ProJet series from 3D Systems, Inc. (which uses the proprietary acronym SLA to refer to SL technology), which routinely produces parts with 50-100  $\mu\text{m}$  resolution in all three axes, and overall dimensions of 0.25-0.5 m. In the most general terms, advancements in SL technology have generally been aimed at achieving four goals: decreasing (1) system cost and (2) minimum feature size (i.e. improving resolution), while (3) increasing overall part size and (4) build speed.

SL systems can be broadly categorized into two classes, by the way in which they deliver illumination to produce the shape of each object layer to be fabricated: laser-scanning and mask projection approaches. Commercially-available SL systems incorporate the laser-scanning approach, following the original scheme described by Hull, since digital image projection technology has only emerged relatively recently as a viable alternative. A significant limitation of laser scanning is the relatively slow speed of rastering the laser to form each layer’s pattern, highlighting the need for a dynamic mask-based approach to polymerize larger areas in a single exposure. The recent proliferation of digital display technologies (referred to as spatial light modulators or SLMs) has enabled the implementation of such “dynamic masking,” increasing system throughput by allowing a complete image layer to be cross-linked simultaneously. These mask projection SL systems are gaining greater prominence, and the landscape of some of the parameters available for system design, as implemented in recent work by a variety of investigators, has been reviewed by Lambert *et al.* [2].

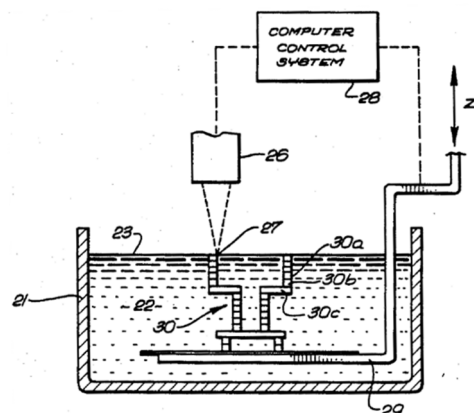


**Figure 1:** Reproduced from US Patent #4575330, by C. Hull, describing the stereolithography (SL) concept. Common features of all SL systems are apparent, including a photocurable resin bath, a computer-controlled light-delivery system, and an elevator supporting the solid 3D part being fabricated.

## 2 Projection Microstereolithography

The projection microstereolithography (P $\mu$ SL) system in operation at Lawrence Livermore National Laboratory (LLNL) that is described in this work incorporates two features unique within the mask projection SL landscape: LED illumination and light patterning using an

LCoS microdisplay. These design parameters support three of the four broad SL development goals mentioned in the first paragraph of Section 1, making significant advancements in cost reduction and feature resolution, and allowing modest gains in build speed.

## 2.1 Unique Features of P $\mu$ SL at LLNL

### 2.1.1 LED Illumination

For selecting an illumination subsystem to deliver light energy in the near-ultraviolet (UV) band typically necessary to cross-link most photopolymer resins (350-400 nm), the main alternative to lasers has been the mercury lamp. Though available at lower cost than most laser sources, such lamps nevertheless cannot be called “low cost,” and their spectral breadth makes them power-intensive and inefficient. However, recent advancements in the development of high-intensity light-emitting diode (LED) arrays capable of near-UV illumination make them an attractive and low-cost alternative. The LLNL P $\mu$ SL system, first described by Zheng *et al.* [3], therefore incorporates a 395-nm LED array (Innovations in Optics) for illumination. The resulting system complexity and cost advantages also extend to the rest of the optical system, since it has substantially less stringent alignment and mechanical stability requirements, compared with laser illumination, and eliminates the extensive filtering and beam-conditioning necessitated by broadband lamps.

### 2.1.2 LCoS Spatial Light Modulator

To generate the dynamic mask for patterning the layer exposure, early mask-projection approaches incorporated liquid crystal displays (LCD) [4], [5], and were followed by the use of digital micromirror devices (DMD) [6]. Most recently, liquid-crystal-on-silicon (LCoS) microdisplay technology has emerged as an improved version of the LCD, with greater reflectivity and improved contrast over transmissive LCDs and more robust than DMDs. For these reasons, our system uses an LCoS microdisplay (Holoeye, HED-6001) to create the digital dynamic mask. In addition to other advantages over LCD and DMD displays, this device has a high pixel-count (1920 $\times$  1080) and 8  $\mu$ m pixel pitch, one of the finest resolutions available on the market to-date. The LED illumination is reflected off the LCoS display (Fig 2) and directed

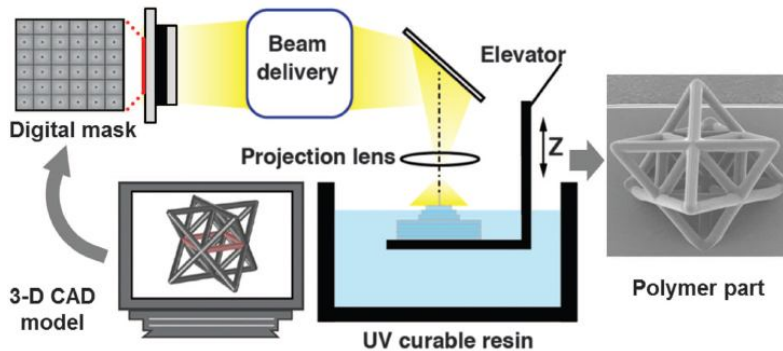


**Figure 2:** Functional schematic of LLNL P $\mu$ SL system. The digital mask is an LCoS microdisplay, which defines the area of the photopolymer to be cured for the current layer. Each image slice is projected by the beam delivery optics onto the resin free surface, as the substrate elevator is gradually lowered into the bath, building the part layer by layer. Reproduced from Ref. [11].

through reduction optics which de-magnify its image approximately seven-fold, for a projection area at the resin surface of about 1.2 $\times$ 2.2 mm, with single-pixel resolution of approx. 1.2  $\mu$ m. Practical minimum features of 10-15  $\mu$ m can be achieved.

### 2.1.3 The PμSL Build Process

The fabrication process begins by “slicing” a 3D CAD model of the desired structure into a stack of binary (black/white) images using a custom script written in python. Each 2D image is displayed on the LCoS microdisplay, and illuminated by UV light from the LED array at a defined intensity and duration. The reflected image projects onto the surface of the polymer resin, for which we most often use HDDA<sup>1</sup> or PEGDA<sup>2</sup>, loaded with 2% (w/w) Irgacure 819<sup>3</sup> as a photoinitiator and 1.2% (w/w) Sudan I<sup>4</sup> as a photoabsorber. The photoabsorber limits the penetration depth of the illumination to 10s of μm, which defines the system’s vertical resolution. The liquid resin exposed to the white areas of the image cures into a solid, and the substrate on which it rests is lowered, reflowing the resin over the cured layer. After raising the substrate again to a predefined depth below the free surface (this determines the thickness of each layer, normally in the range between 5 and 20 μm), the image projection is repeated with subsequent slices, until the desired number of layers has been fabricated to complete the 3D object. A typical 100-layer build takes approximately 70-90 min to complete.

## **2.2 PμSL System Enhancements**

Building upon prior development of this PμSL system at LLNL, I developed three significant system-level advancements which improved process precision and robustness, allowing for more repeatable and reliable production of parts with fewer failed builds, and enabled much of the work described in Section 3 below. These enhancements are real-time focusing feedback, build-time illumination, and ambient oxygen control.

### 2.2.1 Real-time focusing feedback

In order to start a build with the PμSL system, three planes need to be vertically aligned and registered relative to one another. These planes are illustrated in Fig. 3(a), and are (i) the beam reduction optics’ focal plane, (ii)  $z_{bath}$  the free surface of the resin reservoir onto which each layer is projected, and (iii)  $z_{subs}$  the build substrate. The focal plane of the optics is fixed in space, so we refer to this location as  $z = 0$ . The positions of  $z_{bath}$  and  $z_{subs}$  can change from part to part, however, due to substrate changes, resin replenishment or depletion, etc., and therefore require realignment prior to the start of each build. This is carried out by projecting a test pattern, adjusting  $z_{subs}$  until it is in focus on the substrate (kept dry due to the surface tension of the resin), then, after submerging the substrate, adjusting  $z_{bath}$  to focus on the resin surface. After these values are set, a build can proceed using digital stage positioners, which have sub-micron relative positional accuracy.

Previously, build reliability was plagued by a subjective operator-dependent evaluation of when each surface was in focus. From an image-analysis standpoint, attaining proper focus can

---

<sup>1</sup> 1,6-hexanediol diacrylate; CAS #13048-33-4

<sup>2</sup> Poly(ethylene glycol) diacrylate; CAS #26570-48-9

<sup>3</sup> Phenylbis(2,4,6-trimethylbenzoyl) phosphine oxide; CAS #162881-26-7

<sup>4</sup> 1-Phenylazo-2-naphthol; CAS #842-07-9

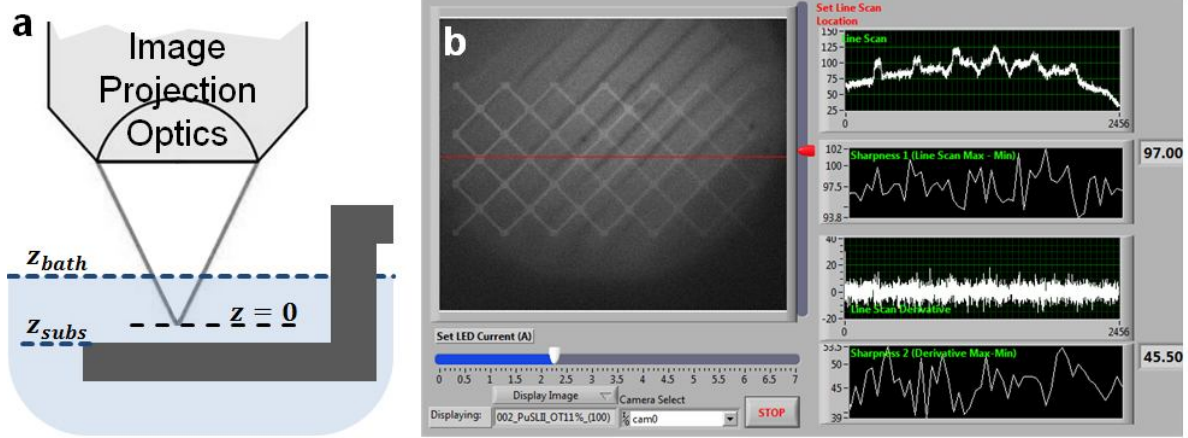


**Figure 3:** User feedback module for pre-build focusing. (a) Schematic of the relevant planes that require positional registration to one another before starting fabrication. (b) The LabVIEW instrument front panel, showing the camera image, an extracted line-scan of image data, and the generated focus parameters  $p_1$  and  $p_2$  displayed in the 2<sup>nd</sup> and 4<sup>th</sup> panels on the right side, respectively.

be defined as maximizing image contrast, or maximizing the sharpness of the edges within an image. However, rather than actually detecting edges, more useful in this context is some single-valued quantitative parameter that can be maximized or minimized to achieve optimal focus.

I therefore implemented real-time processing of the 8-bit (256 gray-values) camera view, shown in Fig. 3(b), to extract a line-scan of the image data at a user-defined location, and calculate two parameters  $p_1$  and  $p_2$  as heuristic image contrast metrics. The first represents the dynamic range of the line-scan itself  $p_1 = I_{max} - I_{min}$  (where  $I$  is the vector of grayscale intensities of the image line-scan), and the second  $p_2 = \delta_{max} - \delta_{min}$  is calculated from a difference-function  $\delta = I_m - I_{m+3}$  that approximates the line-scan derivative at each pixel position  $m$  (the offset value of 3 was chosen empirically). This heuristic approach was chosen, rather than implementing standard edge-detection algorithms like Canny or Sobel methods, since they require more computation, and may fail with the often low-contrast image data of the PuSL system camera view. The simpler calculations of  $p_1$  and  $p_2$  provide the operator with a quantitative real-time assist for the focusing operation at useful data refresh rates (10 Hz or faster). An operator can choose either of the two parameters to maximize, as different substrates and test images will provide optimal performance with one or the other of them. With this module operational, aligning the  $z_{bath}$  and  $z_{subs}$  planes to  $z = 0$  is limited only by the extent of the PuSL optics' depth-of-focus.

### 2.2.2 Build-time illumination

A second desirable system feature for process validation is the ability to observe the part as it is being built. Previously, only the illumination during each layer exposure was available to diagnose the build as it progressed, and determine whether to proceed or abort. I incorporated intensity-adjustable continuous illumination, using high-brightness red LEDs mounted at an oblique-angle, with emission centered at 630 nm, and therefore in a spectral range not absorbed by the photocurable resin. This enabled continuous visualization of the build, during each layer

exposure, as well as between exposures, during stage movements and recoating of the resin, providing verification that the structure is building properly.

### 2.2.3 Ambient Oxygen Control and Substrate Stability

Dissolved oxygen in photosensitive resins is a free-radical scavenger, and inhibits photo-initiated crosslinking reactions until the reaction consumes all available dissolved oxygen. Therefore, free-radical polymerization needs to take place in a low-oxygen or oxygen-free environment. Generally, our system requires oxygen concentration to be reduced approximately 100-fold from atmospheric levels (down to 0.1-0.2% from 20.9%). This is accomplished by flowing a mixture of pure nitrogen ( $N_2$ ) and dry air, at a desired ratio into the chamber. From diffusivity values measured for oxygen in HDDA ( $\sim 10^{-6} \text{ cm}^2/\text{s}$  [7] corresponding to a characteristic diffusion time on the order of 25-50 s to a depth of 100  $\mu\text{m}$ ), we assume equilibration of oxygen with the ambient within a few minutes, in the top layers of resin.

A prototype oxygen-control chamber had been built for the early studies of system parameters [3], but gas mixing was imprecise, and the chamber was not robust, suffering from significant leakage and inducing poor process repeatability. Measurements of  $[O_2]$  in the chamber (NeoFox sensor, Ocean Optics) showed fluctuations of  $\pm 0.08\%$   $[O_2]$  about the nominal value (when no build was in progress), and drifts of 0.1%  $[O_2]$  or more during a build.

To address these shortcomings, I designed and fabricated a tight-tolerance chamber made of solvent-welded acrylic (Figure 4) to control the ambient gas around the resin bath. The design provides for a gas delivery port, as well as feed-throughs for the beam delivery optics, the substrate platform mount, and oxygen sensor probes. I redesigned the substrate mounting hardware and added tip-tilt adjustment

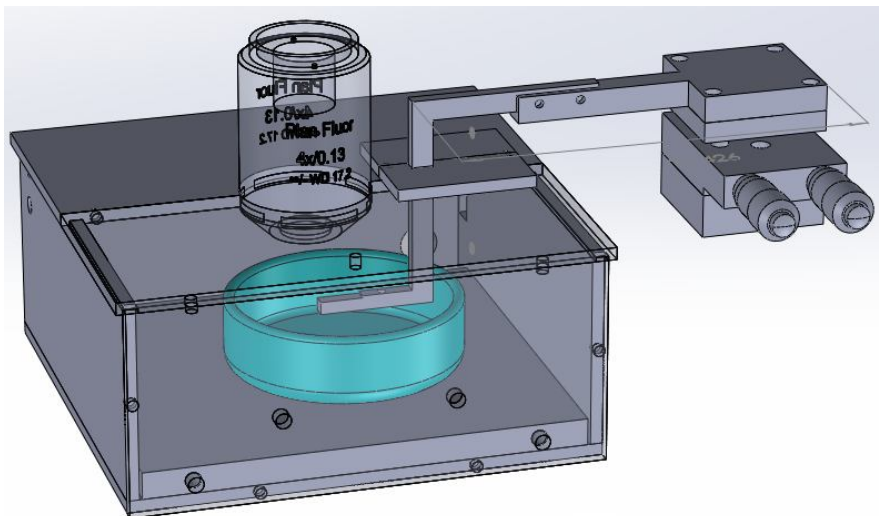


**Figure 4:** 3D model in SolidWorks of the PuSL build chamber and substrate mounting and positioning hardware. The chamber front wall and part of the top are set to be transparent. The final beam-delivery optic enters at the top of the chamber, with the glass dish containing the monomer resin shown in teal. At right is the positioning arm supporting the build substrate, and the tip-tilt leveling adjustment is shown. This tip-tilt assembly mounts to the x-y-z digital positioning stages that control substrate motion during a build.

for leveling of the substrate plane relative to the free surface of the resin bath. Replacing the manually-adjusted gas Rotameters used to control  $[O_2]$  in the chamber, I incorporated mass-flow controllers (MFC) with direct flow readout (MFA5500 series, Omega Engineering) to improve the precision of controlling the incoming gas mixture to approximately 1% of the flow setpoint.



With this chamber configuration, we now automatically have better than 20  $\mu\text{m}$  repeatability of substrate mounting before starting a build. Moreover, the stability of the  $[\text{O}_2]$  readout has improved to  $\pm 0.02\%$ , with the nominal value remaining stable throughout a build.

### 2.3 Polymerization Depth Study

One critical area of ongoing investigation is the development of a comprehensive process model for P $\mu$ SL. The multiplicity of process parameters that affect the geometry of the part being built include delivered light energy dose (i.e. illumination intensity and exposure time), resin photochemistry parameters (such as photoinitiator and photoabsorber concentration and polymerization kinetics), oxygen concentration, as well as layer thickness and substrate-interaction effects. The resulting parts can be characterized by a range of output parameters, including cure depth and shape, degree of cross-linking, and residual stress. Only some of these have been investigated by our group [3], as well as other researchers [8]–[10], and these studies are largely empirical and limited in scope.

A comprehensive and predictive computational model remains to be elucidated. This is important not only for understanding the system performance envelope for well-tested polymer resins, but for successfully extending the available material set into reliable production of metal- and ceramic- loaded parts.

With this goal in mind, enabled by the increased system robustness and reliability, I collected an extensive dataset for characterizing HDDA resin cure-depth as a function of light intensity, exposure, and oxygen concentration. The test structures that I fabricated for this purpose were beams approximately 60  $\mu\text{m}$  wide and 175  $\mu\text{m}$  long, spanning between pillars of square cross-section 125  $\mu\text{m}$  on each side. The pillars were built up to a height of 100  $\mu\text{m}$  such that the beams span the unpolymerized region between them. After exposing each individual beam using specific time/intensity parameters, a new tier was added by building up the support pillars an additional 100  $\mu\text{m}$ . In this way, using several tiers of pillars and beams, the result was a single structure comprising 60 distinct exposure conditions, a subsection of which is shown in Figure 5a. The vertical thickness of each individual beam was measured using a calibrated microscope objective (Fig. 5b), producing a matrix of cure depth values spanning a range of light intensities (6-13  $\text{mW}/\text{cm}^2$ ) and exposure times (6-36 s), corresponding to a delivered energy range from 25 to 250  $\text{mJ}/\text{cm}^2$ . Duplicate structures were built for each set

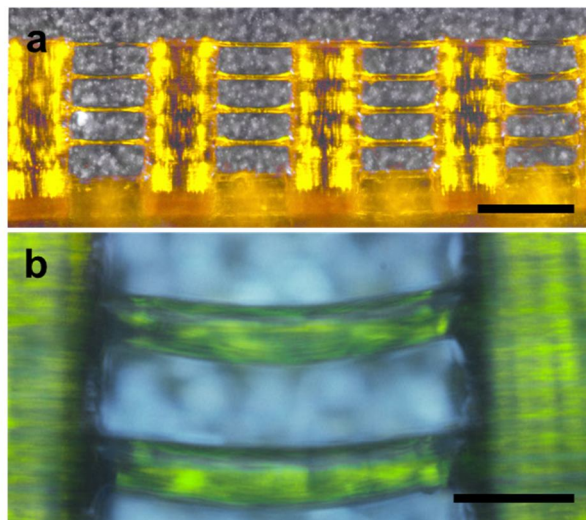


**Figure 5:** Beam and pillar test structures produced by P $\mu$ SL for studying the effects of exposure parameters and ambient oxygen on cure depth. (a) Beams of different thickness due to varied exposure parameters. (b) High-magnification view used to measure beam thickness. Scale bar is 200  $\mu\text{m}$  in (a) and 50  $\mu\text{m}$  in (b).

of 60 exposure conditions at oxygen concentrations of 0.1%, 0.2% and 0.3%, (as measured by relative flow rates from the gas-control MFCs, assuming the incoming air contains 20.9% [O<sub>2</sub>]). For all parts included in this study photoinitiator and photoabsorber loading was 2% Irgacure 819 and 1.2% Sudan I, respectively.

The results of these measurements are summarized in Figure 6. The data follow expected trends, with curing depth  $d$  showing an approximately logarithmic dependence on exposure time and intensity, in rough agreement with the simple analysis from Beluze *et al.* [5] showing that  $d \propto \ln(I_{ex} \cdot t_{ex})$  where  $I_{ex}$  is incident light intensity (mW/cm<sup>2</sup>) and  $t_{ex}$  is exposure time.

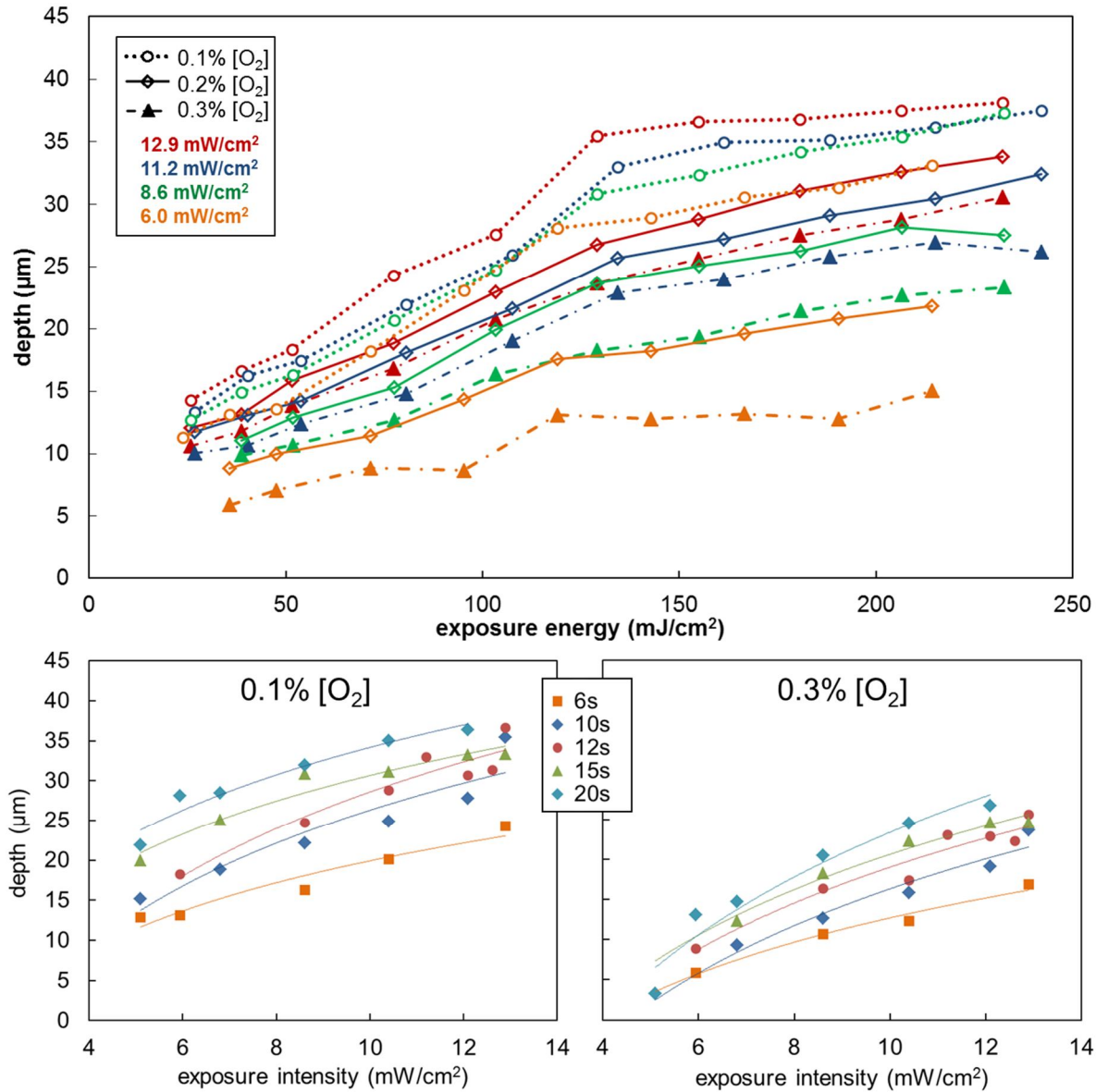


**Figure 6:** Curing depth of HDDA resin with 2% photoinitiator and 1.2% photoabsorber loading. The **top panel** shows cure depth as a function of total exposure energy for different intensities and O<sub>2</sub> concentrations. Symbol shapes and line type denote [O<sub>2</sub>] values, and colors correspond to illumination intensity. The **bottom panels** show selected subsets of the same depth data, with curves of constant exposure time plotted as a function of intensity. Overlaid lines are logarithmic fits to the data, and both depth axes are scaled identically.

However, additional dependencies are immediately apparent, as, for example, exposing at higher intensity produces deeper polymerization for the same total energy delivered. The similar slopes of the logarithmic curves in the bottom plots in Fig 6 suggest that oxygen concentration may determine a scaling pre-factor for the overall dependence on intensity. However, fully understanding the influence of ambient oxygen remains a work in progress. For our specific process, measurements of additional output parameters besides cure depth, especially degree of cross-linking (photoconversion) will provide a fuller understanding on which to base a hybrid analytical-numerical model. Such measurements are currently ongoing.

Fortunately, even in the absence of a fully-developed model, the beam-thickness measurement data serves as a useful calibration matrix for selecting usable process parameters to achieve a desired build. A similar calibration matrix can be generated any time the system is reconfigured (e.g. changes in resin composition or optical realignment).

### 3 Application of P $\mu$ SL to Microarchitected Materials

*The following sections are adapted from Zheng et al. [11], an article published in Science, to which I was a significant contributor and one of two primary writers.*

Development of extremely lightweight materials (<10 kg/m<sup>3</sup>) that are also very strong and stiff is a major scientific and engineering challenge, and the potential for broad impact is increasing due to advances in manufacturing techniques that span multiple length scales. Materials with this elusive combination of properties will have enormous impact in a wide range of fields such as structural components for energy-efficient transportation systems, catalyst supports, biomaterials, and more. A number of prominent papers on the properties of engineered cellular materials [12]–[16], as well as an entire symposium at the Materials Research Society devoted to these topics, point to a high level of interest in this area.

#### 3.1 Mechanical Properties of Low-density Materials

##### 3.1.1 Density-Dependent Scaling of Elastic Modulus and Strength

A key challenge in light-but-strong materials development is that as their density is scaled down (usually by increasing porosity) the degradation in mechanical properties can be dramatic. Recently-reported examples include graphene elastomers [17] and carbon nanotube foams [18]. Another example is silica aerogels [19], [20], for which the Young's modulus decreases to 10<sup>-5</sup>% of the bulk value at a density of < 0.5% of bulk. This loss of mechanical performance is because for most natural and engineered cellular solids with random porosity, properties like Young's modulus and strength, particularly at relative densities less than 0.1%, exhibit a dependence on density that is quadratic or stronger. Namely,  $E/E_s \propto (\rho/\rho_s)^n$  and  $\sigma_y/\sigma_{ys} \propto (\rho/\rho_s)^n$ , where  $E$  is Young's modulus,  $\rho$  is density,  $\sigma_y$  is yield strength, and  $s$  denotes the respective bulk value of the solid constituent material property. The power  $n$  of the scaling relationship between relative material density and the relative mechanical property depends on the material's microarchitecture.

### 3.1.2 Stretch-Dominated Architectures and the Octet Truss

Conventional cellular foam materials with stochastic porosity are known to deform predominantly through bending of their cell walls and struts [21]. This type of deformation results in relative stiffness (modulus) scaling with  $n = 2$  or 3. However, an architecture with members that primarily carry loads under tension or compression (referred to as “stretch-dominated”) is expected to have significantly higher mechanical efficiency. Deshpande, Fleck and Ashby carried out this analysis [22] showing that in order to be stretch-dominated, a structure must satisfy Maxwell’s criterion for static determinacy in rigid trusses,  $b \geq 3j - 6$ , with  $b$  and  $j$  being the number of struts and frictionless joints, respectively. One such architecture is the octet-truss lattice (Shown in Figure 7), which was further analyzed and tested at the mm scale by Deshpande *et al.* [23], showing a theoretically-optimal linear scaling of modulus and strength with relative density  $E/E_s \propto \rho/\rho_s$ .

### 3.1.3 Significance of PuSL-Fabricated Metamaterial Properties

Taking the octet-truss unit cell as the elementary building block for a range of microarchitected materials, the results that we reported in Zheng *et al.* [11] have two significant aspects. First, the persistence at the microscale of the stretch-dominated response to mechanical loading was confirmed by the linear scaling of Young’s modulus and strength with relative density (Figure 8). Similarly noteworthy was the nearly-isotropic behavior of the octet-truss microarchitecture, which maintains the linear  $E \sim \rho$  scaling relationship independent of loading direction. Second, these advantageous mechanical properties were achieved in a breadth of material types, including polymer, metal and ceramic (the last two in both solid and hollow-tube configurations). Additionally, these properties were maintained over three orders of magnitude in relative density from  $0.87 \text{ kg/m}^3$  to  $468 \text{ kg/m}^3$  (corresponding to 0.025–20% relative density), confirming the metamaterial nature of the structure, whose properties are defined by its microarchitecture rather than the composition. Fabricating ordered lattice structures at these length scales brings them into the regime in which it becomes possible to interact with the structure as a material.

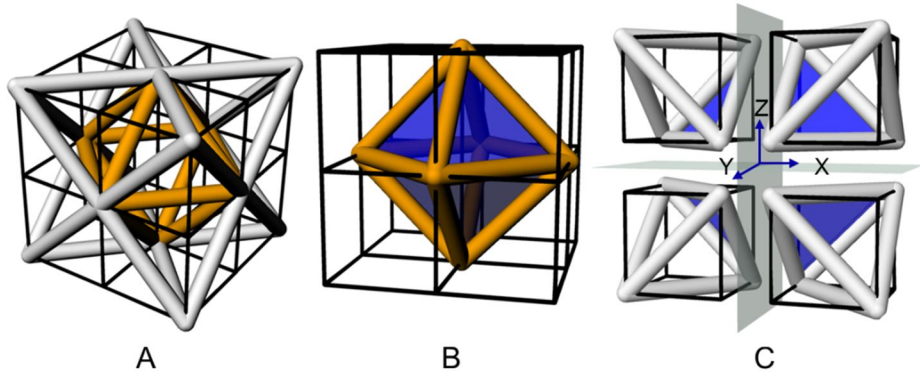


**Figure 7:** The octet-truss lattice unit cell. (A) The structure is face-centered cubic (FCC), comprising a regular octahedron core with regular tetrahedra affixed to each face, resulting in 12 struts connecting at each node (B) The octahedral core of the unit cell with eight symmetry-equivalent faces, corresponding to the eight equivalent orientations in the (111) family. (C) Symmetry of the tetrahedral subunits, and the (111) family of symmetry-equivalent planes. Figure reproduced from Ref. [11]. (Supp. Online Material, Fig. S1).

### 3.2 Breakthrough-Enabling Capability of P $\mu$ SL

P $\mu$ SL, as implemented at LLNL, is one of the few fabrication processes capable of producing the 3D microarchitectures that enable this work. The flexibility and high resolution of the process means that nearly arbitrary geometries with features down to  $\sim 10$   $\mu\text{m}$  can be produced. The photosensitive resin can be loaded with nanoparticles, with the photopolymer removed after cross-linking from the resulting “green body” by thermal decomposition (pyrolysis). This was carried out in this work with 150 nm alumina nanoparticles to produce solid ceramic microlattices (filled red squares in Fig. 8). Furthermore, combining P $\mu$ SL with nano-scale thin film deposition methods provides an additional avenue to incorporating non-polymer materials. By coating a template polymer truss with metal (e.g. electroless Ni-P deposition) or ceramic (e.g.  $\text{Al}_2\text{O}_3$  by atomic layer deposition), then subsequently pyrolyzing the polymer template, hollow-tube microlattices can be produced (open squares in Fig. 8). These structures have wall thickness from 2  $\mu\text{m}$  down to 40 nm, accessing the ultra-low density regime ( $<0.1\%$  relative density).

Although some investigators have described approaches to reduce the 2<sup>nd</sup>- or 3<sup>rd</sup>-order dependence of mechanical properties on relative density [12], [24]–[27], and others have demonstrated improved mechanical properties by designing materials with micro- and nano-scale building blocks within an ordered hierarchy [15], [28], [29], the favorable properties are mostly limited to a narrow density range and specific loading directions. No other methods have been able to access the breadth of material types, nor the large range of relative densities, nor the isotropic properties of the structures made by P $\mu$ SL that enabled this work.

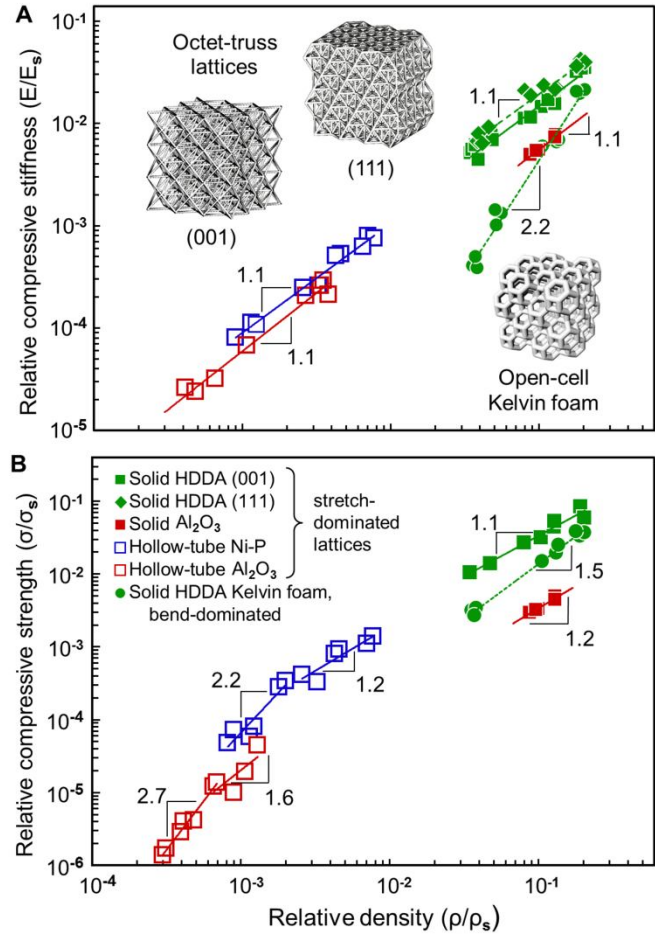


**Figure 8:** The results of uniaxial compressive load testing on a range of octet-truss samples, showing (A) relative stiffness and (B) relative strength as a function of relative density for stretch-dominated and bend-dominated microlattices. Stretch-dominated materials exhibit nearly linear stiffness-density scaling, while bend-dominated materials soften as  $E \sim \rho^2$  or worse, shown by slopes in the plot. The figure is reproduced from [11], where the complete details of mechanical testing are described, as well as the transition from linear to quadratic scaling of strength ultralow density.



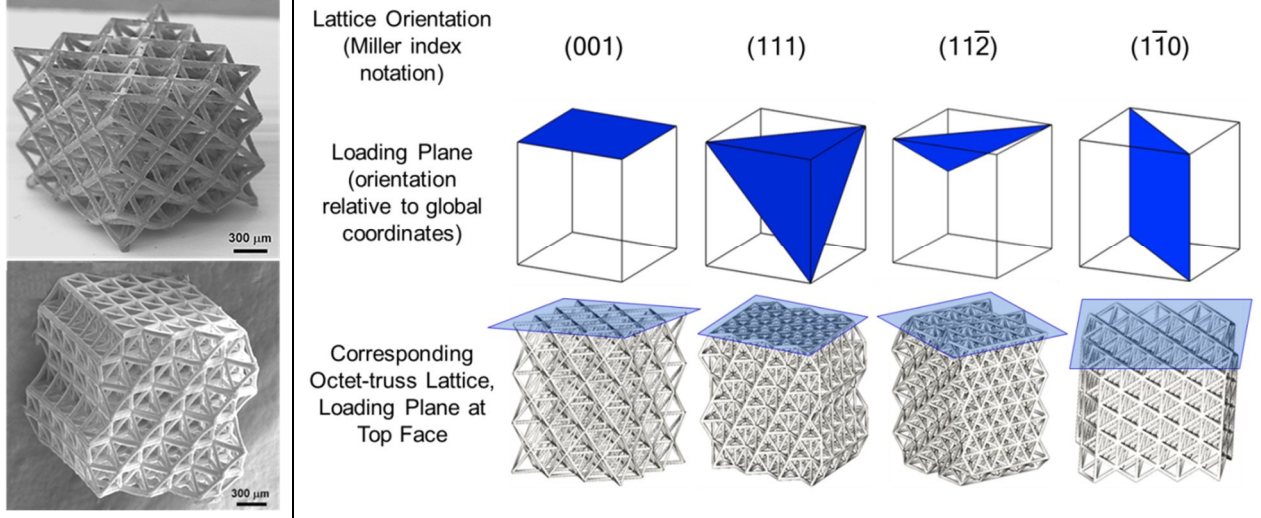


**Figure 9:** Octet-truss lattices fabricated and analyzed in different orientations. The **left panel** shows SEM images of as-built polymer trusses in the (001) and (111) orientation, at 11% relative density. The **right panel** uses CAD models to illustrate the different lattice orientations used for studying structure isotropy under mechanical loading in different directions. The test samples for studying the  $(11\bar{2})$  and  $(1\bar{1}0)$  orientations are produced by rotating the (111) structure  $90^\circ$ .

To study how the truss microarchitecture and loading direction affect the  $E \sim \rho$  scaling relationship, we designed and fabricated octet-truss lattices in a variety of lattice orientations. My contributions to this work were in creating many of the base polymer lattices using PμSL for subsequent post-processing or mechanical testing. This included the initial generation of 3D models of the octet-truss lattices in SolidWorks in the (001) and (111) lattice orientations at a range of relative densities (Figure 9). I then produced the 2D image-sets and build-script input files, and fabricated the required test samples via PμSL. The samples were typically scaled to have exterior dimensions of  $1 \times 1 \times 1 \text{ mm}^3$ , each comprising  $\sim 30$  unit cells. The geometries of the microlattice test samples were likewise used as the basis for finite-element numerical modeling and analysis of the octet-truss architectures.

## 4 Conclusions and Outlook

As a general-purpose AM capability, PμSL provides a flexible platform for a breadth of applications, only one of which is exploring novel material configurations and their properties. One limitation of the current system is its small (mm-scale) build area. Thus, future efforts are needed to address this aspect of the four general AM development goals mentioned in Section 1. System reliability and its ultimate resolution limits can be further enhanced by continuing the effort to develop a PμSL process model predictive capabilities. Furthermore, although we have already demonstrated a broad set of materials in PμSL, expanding the flexibility and versatility of the system, from a constituent materials standpoint, will be of considerable benefit. Along these lines, one potentially fruitful approach is the incorporation of multiple resins in a single build, for example by integrating a flow chamber and valving capability. Of course, many of these advancements will also provide benefit to other SL and AM platforms, including commercially-available systems.

## 5 References

- [1] C. W. Hull, “United States Patent: 4575330 - Apparatus for production of three-dimensional objects by stereolithography,” 4575330, 11-Mar-1986.
- [2] P. M. Lambert, E. A. Campaigne III, and C. B. Williams, “Design Considerations for Mask Projection Microstereolithography Systems,” in *Proceedings of the Solid Freeform Fabrication Symposium*, Austin, TX, 2013, p. 111.
- [3] X. Zheng, J. Deotte, M. P. Alonso, G. R. Farquar, T. H. Weisgraber, S. Gemberling, H. Lee, N. Fang, and C. M. Spadaccini, “Design and optimization of a light-emitting diode projection microstereolithography three-dimensional manufacturing system,” *Rev. Sci. Instrum.*, vol. 83, no. 12, p. 125001, Dec. 2012.
- [4] A. Bertsch, J. Y. Jézéquel, and J. C. André, “Study of the spatial resolution of a new 3D microfabrication process: the microstereophotolithography using a dynamic mask-generator technique,” *J. Photochem. Photobiol. Chem.*, vol. 107, no. 1–3, pp. 275–281, Jul. 1997.
- [5] L. Beluze, A. Bertsch, and P. Renaud, “Microstereolithography: a new process to build complex 3D objects,” in *Design, Test, and Microfabrication of MEMS/MOEMS*, 1999, pp. 808–817.
- [6] C. Sun, N. Fang, D. M. Wu, and X. Zhang, “Projection micro-stereolithography using digital micro-mirror dynamic mask,” *Sens. Actuators Phys.*, vol. 121, no. 1, pp. 113–120, May 2005.
- [7] A. K. O’Brien and C. N. Bowman, “Impact of Oxygen on Photopolymerization Kinetics and Polymer Structure,” *Macromolecules*, vol. 39, no. 7, pp. 2501–2506, Apr. 2006.
- [8] N. Fang, C. Sun, and X. Zhang, “Diffusion-limited photopolymerization in scanning microstereolithography,” *Appl. Phys. A*, vol. 79, no. 8, Dec. 2004.
- [9] D. Dendukuri, P. Panda, R. Haghgooei, J. M. Kim, T. A. Hatton, and P. S. Doyle, “Modeling of Oxygen-Inhibited Free Radical Photopolymerization in a PDMS Microfluidic Device,” *Macromolecules*, vol. 41, no. 22, pp. 8547–8556, Nov. 2008.
- [10] J. B. Mueller, J. Fischer, F. Mayer, M. Kadic, and M. Wegener, “Polymerization Kinetics in Three-Dimensional Direct Laser Writing,” *Adv. Mater.*, vol. 26, no. 38, pp. 6566–6571, Oct. 2014.
- [11] X. Zheng, H. Lee, T. H. Weisgraber, M. Shusteff, J. DeOtte, E. B. Duoss, J. D. Kuntz, M. M. Biener, Q. Ge, J. A. Jackson, S. O. Kucheyev, N. X. Fang, and C. M. Spadaccini, “Ultralight, ultrastiff mechanical metamaterials,” *Science*, vol. 344, no. 6190, pp. 1373–1377, Jun. 2014.
- [12] T. A. Schaedler, A. J. Jacobsen, A. Torrents, A. E. Sorensen, J. Lian, J. R. Greer, L. Valdevit, and W. B. Carter, “Ultralight Metallic Microlattices,” *Science*, vol. 334, no. 6058, pp. 962–965, Nov. 2011.
- [13] D. Jang, L. R. Meza, F. Greer, and J. R. Greer, “Fabrication and deformation of three-dimensional hollow ceramic nanostructures,” *Nat. Mater.*, vol. 12, no. 10, pp. 893–898, Sep. 2013.
- [14] K. C. Cheung and N. Gershenfeld, “Reversibly Assembled Cellular Composite Materials,” *Science*, vol. 341, no. 6151, pp. 1219–1221, Sep. 2013.
- [15] J. Bauer, S. Hengsbach, I. Tesari, R. Schwaiger, and O. Kraft, “High-strength cellular ceramic composites with 3D microarchitecture,” *Proc. Natl. Acad. Sci.*, vol. 111, no. 7, pp. 2453–2458, Feb. 2014.
- [16] L. R. Meza, S. Das, and J. R. Greer, “Strong, lightweight, and recoverable three-dimensional ceramic nanolattices,” *Science*, vol. 345, no. 6202, pp. 1322–1326, 2014.
- [17] L. Qiu, J. Z. Liu, S. L. Y. Chang, Y. Wu, and D. Li, “Biomimetic superelastic graphene-based cellular monoliths,” *Nat. Commun.*, vol. 3, p. 1241, Dec. 2012.
- [18] M. A. Worsley, S. O. Kucheyev, J. H. Satcher, A. V. Hamza, and T. F. Baumann, “Mechanically robust and electrically conductive carbon nanotube foams,” *Appl. Phys. Lett.*, vol. 94, no. 7, p. 073115, 2009.
- [19] T. M. Tillotson and L. W. Hrubesh, “Transparent ultralow-density silica aerogels prepared by a two-step sol-gel process,” Lawrence Livermore National Lab., CA (United States), 1991.

- [20] S. O. Kucheyev, M. Stadermann, S. J. Shin, J. H. Satcher, S. A. Gammon, S. A. Letts, T. van Buuren, and A. V. Hamza, “Super-Compressibility of Ultralow-Density Nanoporous Silica,” *Adv. Mater.*, vol. 24, no. 6, pp. 776–780, 2012.
- [21] L. J. Gibson, “Cellular solids,” *Mrs Bull.*, vol. 28, no. 04, pp. 270–274, 2003.
- [22] V. S. Deshpande, M. F. Ashby, and N. A. Fleck, “Foam topology: bending versus stretching dominated architectures,” *Acta Mater.*, vol. 49, no. 6, pp. 1035–1040, Apr. 2001.
- [23] V. S. Deshpande, N. A. Fleck, and M. F. Ashby, “Effective properties of the octet-truss lattice material,” *J. Mech. Phys. Solids*, vol. 49, no. 8, pp. 1747–1769, Aug. 2001.
- [24] H. Fan, C. Hartshorn, T. Buchheit, D. Tallant, R. Assink, R. Simpson, D. J. Kissel, D. J. Lacks, S. Torquato, and C. J. Brinker, “Modulus–density scaling behaviour and framework architecture of nanoporous self-assembled silicas,” *Nat. Mater.*, vol. 6, no. 6, pp. 418–423, Jun. 2007.
- [25] K. Tantikom, Y. Suwa, and T. Aizawa, “In-plane compression response of regularly cell-structured materials,” *Mater. Trans.*, vol. 45, no. 2, pp. 509–515, 2004.
- [26] C. Q. Dam, R. Brezny, and D. J. Green, “Compressive behavior and deformation-mode map of an open cell alumina,” *J. Mater. Res.*, vol. 5, no. 01, pp. 163–171, 1990.
- [27] D. Rayneau-Kirkhope, Y. Mao, and R. Farr, “Ultralight Fractal Structures from Hollow Tubes,” *Phys. Rev. Lett.*, vol. 109, no. 20, Nov. 2012.
- [28] A. Torrents, T. A. Schaedler, A. J. Jacobsen, W. B. Carter, and L. Valdevit, “Characterization of nickel-based microlattice materials with structural hierarchy from the nanometer to the millimeter scale,” *Acta Mater.*, vol. 60, no. 8, pp. 3511–3523, May 2012.
- [29] L. R. Meza and J. R. Greer, “Mechanical characterization of hollow ceramic nanolattices,” *J. Mater. Sci.*, vol. 49, no. 6, pp. 2496–2508, Mar. 2014.

This work was performed under the auspices of the U.S. Department of Energy by Lawrence Livermore National Laboratory under Contract DE-AC52-07NA27344. LLNL-TR-666552